ACS APPLIED MATERIALS & INTERFACES

www.acsami.org

Research Article

Probing the Atomic-Scale Structure of Amorphous Aluminum Oxide Grown by Atomic Layer Deposition

Matthias J. Young,* Nicholas M. Bedford, Angel Yanguas-Gil, Steven Letourneau, Matthew Coile, David J. Mandia, Bachir Aoun, Andrew S. Cavanagh, Steven M. George, and Jeffrey W. Elam*

Cite This: *ACS Appl. Mater. Interfaces* 2020, 12, 22804–22814

Read Online

ACCESS | Metrics & More | Article Recommendations

ABSTRACT: Atomic layer deposition (ALD) is a well-established technique for depositing nanoscale coatings with pristine control of film thickness and composition. The trimethylaluminum (TMA) and water (H_2O) ALD chemistry is inarguably the most widely used and yet to date, we have little information about the atomic-scale structure of the amorphous aluminum oxide (AlO_x) formed by this chemistry. This lack of understanding hinders our ability to establish process−structure−property relationships and ultimately limits technological advancements employing AlO_x made *via* ALD. In this work, we employ synchrotron high-energy X-ray diffraction (HE-XRD) coupled with pair distribution function (PDF) analysis to characterize the atomic structure of amorphous AlO_x ALD coatings. We combine *ex situ* and *in operando* HE-XRD measurements on ALD AlO_x and fit these experimental data using stochastic structural modeling to reveal variations in the Al−O bond length, Al and O coordination environment, and extent of Al vacancies as a function of growth conditions. In particular, the local atomic structure of ALD AlO_x is found to change with the substrate and number of ALD cycles. The observed trends are consistent with the formation of bulk Al_2O_3 surrounded by an O-rich surface layer. We deconvolute these data to reveal atomic-scale structural information for both the bulk and surface phases. Overall, this work demonstrates the usefulness of HE-XRD and PDF analysis in improving our understanding of the structure of amorphous ALD thin films and provides a pathway to evaluate how process changes impact the structure and properties of ALD films.

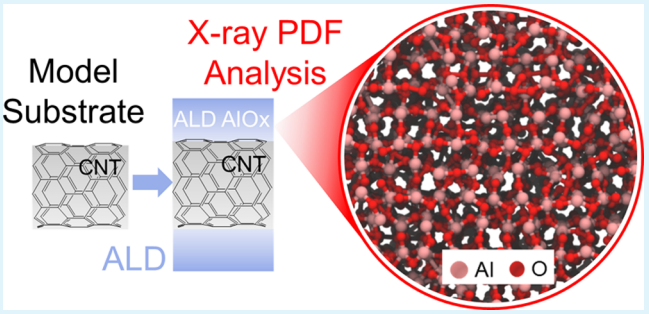

KEYWORDS: *ALD, Al_2O_3, synchrotron, in operando, HE-XRD, PDF analysis, amorphous, atomic structure*

1. INTRODUCTION

The ability to grow conformal films with atomic-scale control of thickness and composition makes atomic layer deposition (ALD) an attractive means of protecting and/or chemically functionalizing surfaces for catalysis,[1,2] energy storage,[3,4] photoelectrochemistry,[5,6] quantum computing devices,[7] and other applications. ALD is also scalable, with uniform thin-film coatings on particles achievable at >3 ton/day scale[8] and routine use of ALD in semiconductor device manufacturing.[7] However, the performance of ALD coatings in areas of emerging research interest frequently falls short of expectations. This difficulty in expanding ALD into new research spaces is arguably because of the lack of detailed understanding of the atomic structure that governs the chemical and physical properties of ALD films. Single-crystal materials are rarely achievable by ALD.[9] More often, ALD films form amorphous, polycrystalline, or defective structures. ALD process conditions such as precursor selection(s), precursor exposure(s), and reactor temperature are known to affect the growth mechanism and properties of resulting films.[10−15] The substrate also impacts the properties of ALD films.[16−18] To date, the ALD community has been unable to connect atomic structural changes in ALD films with the performance of the resulting material, largely because of an inability to determine the atomic structure of the ALD films. As a result, it is often the case that only select "champion" examples of ALD-grown materials exhibit desired properties. To improve the performance of ALD films for the applications mentioned above, we need to close the loop on the process−structure−property relationships for ALD growth by establishing techniques to characterize the atomic structure of amorphous, polycrystalline, and defective ALD structures.

Amorphous aluminum oxide (AlO_x) grown using trimethylaluminum (TMA) and water (H_2O) is the most ubiquitous ALD chemistry[13] with >1000 papers reported in Google

Received: January 31, 2020
Accepted: April 20, 2020
Published: April 20, 2020

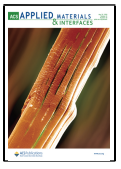

https://dx.doi.org/10.1021/acsami.0c01905
ACS Appl. Mater. Interfaces 2020, 12, 22804−22814

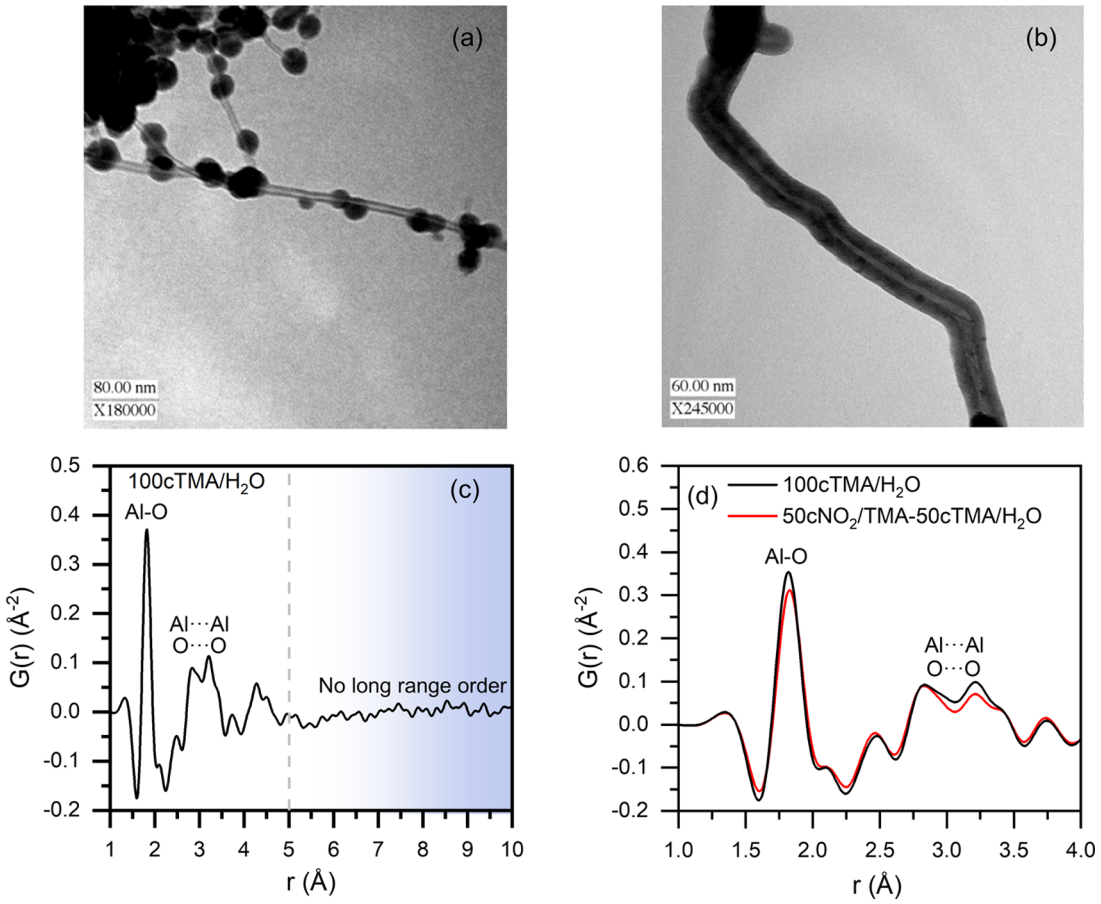

Figure 1. Transmission electron microscopy images for (a) 100 ALD cycles of TMA/H_2O and (b) 50 nucleation cycles of NO_2/TMA followed by 50 ALD cycles of TMA/H_2O deposited at 180 °C on nonfunctionalized CNTs (adapted with permission from ref 44) along with PDFs derived from HE-XRD measurements of (c) 100 ALD cycles of TMA/H_2O showing no long-range order, and (d) local structure comparison against 50 nucleation cycles of NO_2/TMA followed by 50 ALD cycles of TMA/H_2O with a narrower *x*-axis range *vs* (c) to improve visibility of peaks.

Scholar each year employing this chemistry, as identified using the search query phrase "("ALD" or "atomic layer deposition"), ("trimethylaluminum" or "TMA"), and ("water" or "H_2O")". Although the surface chemistry,[13,14] composition,[14,19] and microstructure[20,21] of ALD AlO_x have been evaluated in prior work, little data on the atomic-scale structural features of ALD AlO_x are available beyond traditional amorphous *versus* polycrystalline classification.[11,22−24] Although the atomic-scale structure of AlO_x has been studied for bulk[25,26] and micron-scale films[27] deposited by other techniques, these studies do not necessarily reflect the structure of ALD films. One of the main advantages of ALD is the ability to selectively modify the surface properties of a material, and as such, target ALD aluminum oxide thicknesses are commonly <10 nm. At these ultrathin film thicknesses, one reasonably expects that the atomic structure of ALD aluminum oxide differs from thicker film or bulk aluminum oxide. Furthermore, ALD is known to enable access to metastable phases,[28] and specific ALD process conditions may drive differences in the atomic structure over other deposition processes. Although solid-state nuclear magnetic resonance (NMR) has been used to characterize the atomic structure of bulk amorphous aluminum oxide[25−27] and to study ALD films on high surface area powder substrates,[29−31] a number of factors limit the insights it can provide. For example, NMR is limited in the elements which can be probed (*i.e.*, only NMR active elements), in the substrates which can be employed (*e.g.*, nonmagnetic), and in the sample quantity and geometry (*e.g.*, milligram quantities confined in an NMR tube within a high-field magnet). In particular, NMR is infeasible to perform *in operando* during ALD deposition, as we report here. We also note that electron energy loss spectroscopy has been performed on ALD-grown aluminum oxide,[32] but electron beam damage during these measurements[33] limits the relevance of these results.

Here, we employ synchrotron high-energy X-ray diffraction (HE-XRD) coupled with pair distribution function (PDF) analysis to characterize the atomic structure of amorphous aluminum oxide. HE-XRD and PDF analysis is fit-for-purpose to provide atomic-scale structural information in ALD aluminum oxide. PDF analysis provides access to the atomic-scale structural features with sub-Angstrom resolution across large atomic-pair distances (>∼40 Å),[34] yielding structural insights such as bond lengths and coordination numbers (CNs). PDFs are generated from HE-XRD patterns through the Fourier transform of both diffuse and Bragg components of the scattering data. The resulting PDFs provide structural information for all elements present in terms of atomic pairs irrespective of the presence of long-range order, allowing for atomic structure determination of amorphous[34−38] and nanoscale materials.[35,37,39] Prior work from our group and others has employed PDF analysis to probe the atomic structures of thin films of high-Z materials and/or materials which exhibit long-range order such as W, MoS_2, ZrO_2, Ta_2O_5 and HfO_2.[40−43] In the present work, we demonstrate the use of

https://dx.doi.org/10.1021/acsami.0c01905
ACS Appl. Mater. Interfaces 2020, 12, 22804−22814

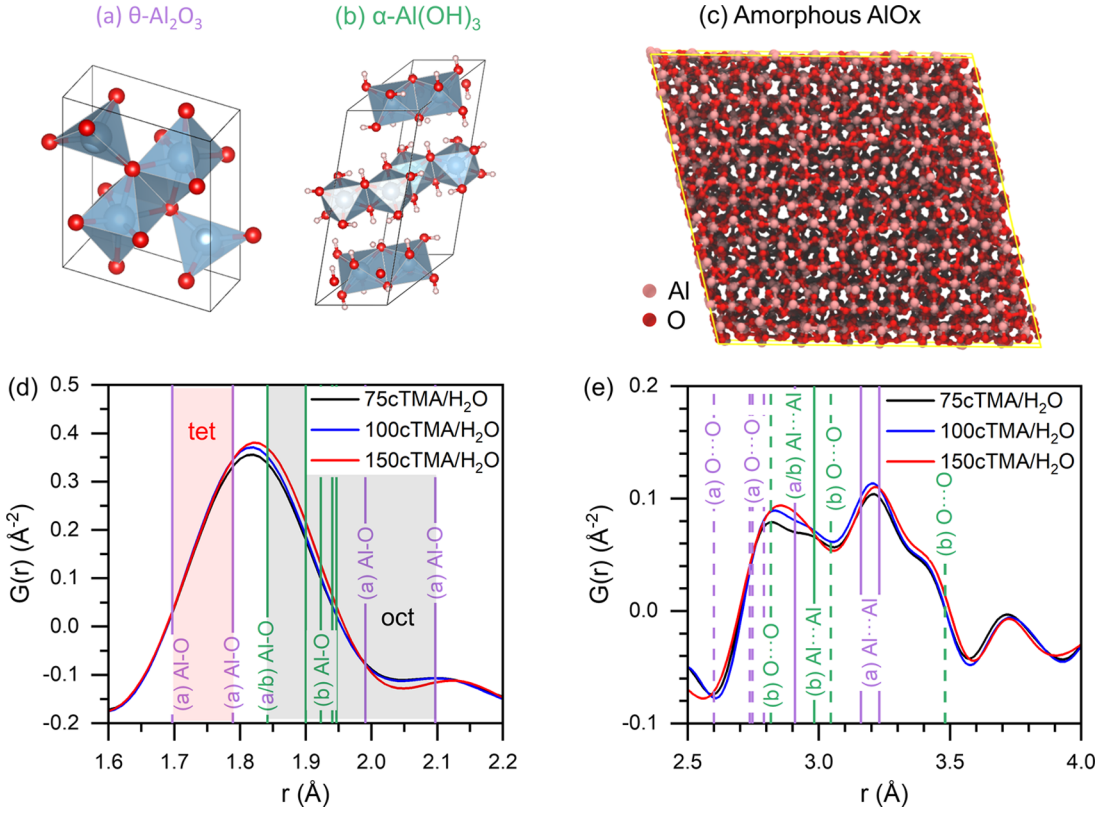

Figure 2. Reference ideal crystal structures of (a) θ-Al_2O_3 and (b) α-$Al(OH)_3$ used for qualitative evaluation of PDF data along with the (c) an example of a stochastic structural model, all of which were used to interpret variations in PDF data from 75cTMA/H_2O, 100cTMA/H_2O, and 150cTMA/H_2O ALD films, especially in the (d) Al−O bonding distance region and (e) Al···Al and O···O coordination pair distance region.

synchrotron HE-XRD coupled with PDF analysis to characterize the atomic structure of low-Z and amorphous aluminum oxide both *ex situ* and *in operando* during ALD growth. The procedures and insights we report provide a platform to establish process−structure−property relationships for ALD aluminum oxide and ultimately enable rational control of matter at the nanoscale to enable advanced technologies.

2. RESULTS AND DISCUSSION

In Figure 1, we depict TEM micrographs and the corresponding PDF data from *ex situ* HE-XRD measurements for carbon nanotube (CNT) samples coated with ALD AlO_x at 180 °C. Figure 1a shows 100 ALD cycles of TMA/H_2O grown on CNTs with no nucleation layer, while Figure 1b depicts 40 ALD cycles of TMA/H_2O grown on CNTs with 50 cycles of NO_2/TMA nucleation pretreatment, as described in previous work.[44] Without a nucleation pretreatment (Figure 1a), the TMA/H_2O nucleates on defects in the CNT, producing beads of AlO_x on the order of 20 nm in diameter distributed along the CNT surface. With the NO_2/TMA nucleation pretreatment (Figure 1b), a uniform thin film of AlO_x is deposited on the CNT surface.[44,45] One may expect that the differences in nucleation between these two samples may lead to differences in the local atomic structure of the AlO_x and therefore impact the properties of the film.

In order to probe the local structure of the amorphous AlO_x, we employ HE-XRD and PDF analysis. In Figure 1c, we present the PDF of 100 ALD cycles of TMA/H_2O grown on CNTs with no nucleation layer (100cTMA/H_2O), as depicted in Figure 1a. The PDF, $G(r)$, is defined as

$$G(r) = \frac{2}{\pi}\int_{Q_{min}}^{Q_{max}} Q[S(Q) - 1]\sin(Qr)dQ$$
$$= 4\pi r[\rho(r) - \rho_0]$$

where r is the atomic pair distance, ρ_0 is the average pair density in the material, $\rho(r)$ is the pair density at a pair distance of r, $Q = 4\pi \sin\theta/\lambda$ is momentum transfer, and $S(Q)$ is the structure function which can be determined from 2D HE-XRD scattering data. Q_{min} and Q_{max} correspond to the experimental Q range over which the scattering data are integrated. In a plot of $G(r)$ *vs* r, a peak in $G(r)$ corresponds to a density of pairs at that pair distance which is greater than the average pair density. For example, the peak in Figure 1c at a pair distance of ∼1.8 Å corresponds to Al−O bonds, whereas the two peaks at around ∼3 Å correspond to Al···Al and O···O atomic pairs. We do not observe peaks in $G(r)$ for r > 5 Å, suggesting that the ALD-grown AlO_x is amorphous, in line with established descriptions of ALD-grown aluminum oxide.[11,22−24] In Figure 1d, we compare the PDFs for the 100cTMA/H_2O sample and a sample with 50 NO_2/TMA nucleation cycles followed by 50 ALD cycles of TMA/H_2O (50cNO_2/TMA-50cTMA/H_2O). In Figure 1d, we observe distinct differences in the PDFs for the materials grown with and without nucleation pretreatment. This finding indicates that there are differences in the atomic-scale structure between two AlO_x materials that would traditionally be classified as just amorphous. The larger area under the peaks at pair distances of ∼1.8 and ∼3.2 Å for the 100cTMA/H_2O sample suggest more highly coordinated Al metal centers and AlO_x clusters, respectively, when no nucleation layer is present. We also

https://dx.doi.org/10.1021/acsami.0c01905
ACS Appl. Mater. Interfaces 2020, 12, 22804−22814

Table 1. Atomic Structure Metrics for Amorphous ALD Aluminum Oxide Deposited by 75cTMA/H_2O, 100cTMA/H_2O, and 150cTMA/H_2O as Derived from Statistical Analysis of Stochastic Structure Models of Experimental PDFs, along with Expected Metrics for Surface $-(R-O)_x-Al-(OH)_y$ Groups and Ideal θ-Al_2O_3 and α-$Al(OH)_3$ Phases

	75cTMA/H_2O	100cTMA/H_2O	150cTMA/H_2O	$(-R-)-Al-(OH)_y$	θ-Al_2O_3	α-$Al(OH)_3$
O/Al	1.662	1.658	1.620	3	1.5	3.0
Al−O (Å)	1.819	1.819	1.820	–	1.87	1.90
Al−O CN	4.58	4.62	4.67	3	5	6
O−Al CN	2.76	2.79	2.88	1−2	3.5	2

observe that the Al−O peak center is at r = 1.818 Å for the 100cTMA/H_2O sample and at r = 1.829 for the 50cNO$_2$/TMA-50cTMA/H_2O condition. This indicates that the Al−O bonds in the 50cNO$_2$/TMA-50cTMA/H_2O sample are longer on average than the Al−O bonds in the 100cTMA/H_2O sample. The differences between the PDFs for the two samples in Figure 1d led us to hypothesize that the size of AlO_x domains may drive local structural differences in the amorphous aluminum oxide.

To evaluate this, we performed HE-XRD and PDF analysis to measure the atomic structure of AlO_x at varying numbers of TMA/H_2O deposition cycles without a NO_2/TMA nucleation layer. In Figure 2, we compare select regions of the experimental PDF data for 75, 100, and 150 TMA/H_2O ALD deposition cycles performed at 180 °C with no nucleation layer (corresponding to Figure 1a). We emphasize that the traces in Figure 2 are average curves calculated from multiple HE-XRD measurements and that the differences between traces in Figure 2 are statistically significant and represent substantial structural differences. For example, over the region of the pair distance from 1.8 to 1.9 Å (Figure 2a), we observe an average difference between the $G(r)$ traces for 75cTMA/H_2O and 150cTMA/H_2O of 0.031 Å^{-2}, which is more than an order of magnitude larger than the average standard deviation of each trace over this region (0.004 Å^{-2} for the 150cTMA/H_2O sample and 0.0009 Å^{-2} for the 75cTMA/H_2O sample). In order to interpret the differences in $G(r)$ we observe with varying numbers of TMA/H_2O ALD cycles, we first referenced these PDFs against pair distances found in ideal unit cell structures of θ-Al_2O_3 (Figure 2a) and α-$Al(OH)_3$ (Figure 2b).[46,47] These ideal crystal structures, among other potential phases,[48,49] are expected to represent local regions of the atomic structure present in the aluminum oxide deposited by ALD. We note that no individual crystalline phase is expected to capture the ensemble structure of amorphous ALD aluminum oxide but that a representative structure capturing the diversity of chemical environments in ALD-derived AlO_x can be obtained using stochastic modeling. Figure 2c is an example stochastic structural model of ALD AlO_x, which was fit against the experimental data for the PDF for 100 cycles of TMA/H_2O grown on nonfunctionalized CNTs. This structural model will be discussed in more detail below. Figure 2d,e highlights PDF regions corresponding to the Al−O (1.6−2.2 Å) and Al···Al/O···O (2.5−4.0 Å) pair distances, respectively. In Figure 2d,e, we also include vertical lines at ideal pair distances present in the two reference crystal structures depicted in Figure 2a,b. We see that these two reference crystal structures exhibit pair distances consistent with our experimental data for ALD-grown AlO_x. We note that we also considered the thermodynamic ground-state corundum-type α-Al_2O_3 structure, but the atomic pair distances for Al···Al pairs within the α-Al_2O_3 structure are at 2.68 and 3.88 Å.[50] Because we do not observe peaks in the experimental PDF for ALD AlO_x in this region, we omitted reference pair distances for the α-Al_2O_3 structure in Figure 2.

Comparing the experimental PDFs for varying numbers of ALD cycles against the ideal reference structures, we are able to reveal insights into how the atomic structure develops during ALD growth. In Figure 2c, we identify that the experimental Al−O pairs present in the ALD-grown sample span a range of pair distances representative of both θ-Al_2O_3 and α-$Al(OH)_3$, where the peak center for the Al−O bonds in the experimental $G(r)$ trace falls between the values expected for tetrahedral and octahedral aluminum metal centers in these aluminum oxide/hydroxide structures. Based on this observation, we expect a combination of both tetrahedral and octahedral aluminum centers in our experimental sample. We also observe that as the film thickness increases from 75 ALD cycles (~8 nm) to 150 ALD cycles (~18 nm), we observe an increase in $G(r)$ for the Al−O peak over the range from 1.8 to 2.0 Å. In the ideal crystal structure of θ-Al_2O_3, tetrahedral Al−O bonds occur at 1.70 and 1.79 Å, while octahedral Al−O bonds occur at 1.99 and 2.10 Å, resulting in an average Al−O bond length of 1.87 Å.[46] In the α-$Al(OH)_3$ crystal structure, a range of octahedral Al−O bonds occur between 1.84 and 1.95 Å with an average Al−O bond distance of 1.90 Å.[47] Based on these values, the increase in $G(r)$ at longer Al−O pair distances with increasing thickness suggests that more octahedral Al metal centers are present in the ALD AlO_x film as the film thickness increases. Similarly, in Figure 2e, we plot $G(r)$ over a range of pair distances from 2.5 to 4 Å, corresponding to the Al···Al and O···O coordination spheres. We note that the increase in $G(r)$ at r = 2.9 Å for larger numbers of ALD aluminum oxide cycles, as shown in Figure 2e, is in line with an increase in octahedral aluminum metal centers.

Although this method of comparison against peak locations in ideal crystal structures is useful, it provides only qualitative insights and has some limitations. For example, we note that the peaks in $G(r)$ observed between 2.6 and 3.6 Å, as shown in Figure 2e, are the superposition of multiple Al···Al and O···O features. The analysis mentioned above suggests that an increase in $G(r)$ over the range of pair distances from 2.8 to 3.0 Å indicates a higher density of octahedral aluminum metal centers. However, Al−O octahedra are present in both the θ-Al_2O_3 and α-$Al(OH)_3$ structures, and this peak could also reasonably arise from higher O···O coordination not observed in either of these structures. The distinction in how to interpret the increase in the feature over the range of pair distances from 2.8 to 3.0 within the larger amorphous structural framework is lost using this simple analysis of peak height and location. We expand upon this qualitative interpretation and extract quantitative comparisons in the atomic structure of the ALD-grown films by employing stochastic structural modeling. Here, the positions of atoms within a model structure simulation box are allowed to vary until the computed PDF from the model structure matches the experimentally measured PDF. Modeling

https://dx.doi.org/10.1021/acsami.0c01905
ACS Appl. Mater. Interfaces 2020, 12, 22804−22814

the data in this way requires the model to be consistent with the experimental data across the whole modeling volume. This process results in stochastic structures representing an ensemble average atomic structure of the material, such as the atomic structure depicted in Figure 2c. We can then evaluate the distribution of local atomic structures within the fitted stochastic structure using statistical analysis to provide quantitative comparisons between the local atomic structure of these ALD films. We note that hydrogen was omitted from the structural models because the X-ray scattering cross section is sufficiently small for hydrogen that the contribution to the HE-XRD pattern is negligible. Future work employing neutron scattering may help reveal the structural contributions of hydrogen.

Reported in Table 1 are values of the oxygen to aluminum stoichiometric ratio (O/Al), average Al−O bond lengths, and CNs derived from statistical analysis of stochastic structures for the three samples measured in Figure 2. We note that the ability to predict the stoichiometric ratio by PDF analysis is enabled by a custom feature within fullrmc which was developed specifically for this work, allowing for atom removal as a structural perturbation step. The ability to change the overall stoichiometric composition in this way enabled prediction of ensemble average stoichiometries reported here. When interpreting the metrics reported in Table 1, it is helpful to consider the expected metrics during initial nucleation of TMA/H_2O reactions at the surface of the CNT (and at the outer terminus of the aluminum oxide domain). At this outer surface, we expect the formation of isolated surface −R−O−Al−$(OH)_2$ and $(-R-O)_2$−Al(OH) groups, as depicted in Figure 3a, where R indicates a site on the surface of the CNT

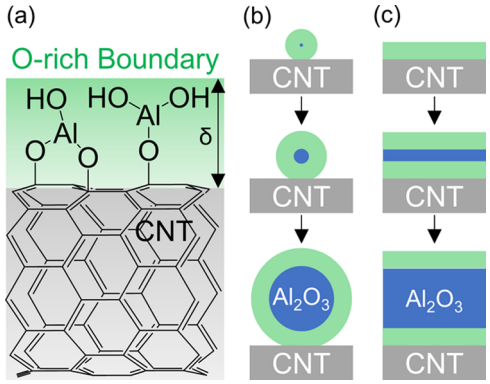

Figure 3. Schematic model depiction used to explain variation in atomic structure with the number of ALD cycles consisting of (a) an O-rich interfacial boundary layer, which surrounds near-stoichiometric bulk Al_2O_3 in both (b) nanoparticle growth and (c) thin-film growth by ALD.

(or the outer aluminum oxide boundary). The bond lengths of these surface groups are unknown, but within these groups, the O/Al ratio is expected to be 3, the Al−O CN is expected to be 3, and the O−Al CN is expected to be 1−2—in line with the schematic depiction in Figure 3a. We have included these values for reference in Table 1 along with average values of metrics for the ideal structures of θ-Al_2O_3 and α-$Al(OH)_3$.[46,47] In Table 1, the O/Al value decreases from 1.662 for 75cTMA/H_2O to 1.620 for 150cTMA/H_2O, corresponding to $Al_{1.80}O_3$ and $Al_{1.85}O_3$, respectively. These values are close to the Al_2O_3 stoichiometry, but are 7−10% deficient in Al relative to Al_2O_3. This modeled Al deficiency in all of these ALD AlO_x samples may arise either from undercoordinated surface Al species or bulk Al vacancies in the AlO_x.

To distinguish between these two possible sources of Al deficiency, we examine these data in light of prior reports on ALD AlO_x. If bulk Al vacancies are present in the ALD AlO_x structure, we would expect a stoichiometric number of protons to be present in the aluminum oxide to maintain the overall charge balance. However, from previous work, a proton concentration of only about 5% is present in ALD aluminum oxide grown at 180 °C,[14] about half of the amount needed to account for the stoichiometry observed here. Conversely, prior reports have observed an O-rich layer at the interfaces of ALD AlO_x,[14,19] consistent with undercoordinated surface Al. We therefore suggest that the excess oxygen we observe may arise because of the nanoscale dimensions of the aluminum oxide—where an O-rich layer of constant thickness, δ, exists at the boundaries of the ALD aluminum oxide and surrounds a near-stoichiometric Al_2O_3 core, as depicted in Figure 3. We expect that these O-rich regions would exist both at the boundary of the CNT interface oxide where ALD growth nucleates and at the exterior boundary surface of the ALD aluminum oxide. We note that such an O-rich outer layer would be expected to produce a negative surface charge for ALD AlO_x, in line with prior observations.[51] Within this proposed O-rich surface layer model, we expect that as growth proceeds, either from nucleation on point defects (Figure 3b) or uniform nucleation and growth over a surface (Figure 3c), the surface area to volume ratio of the aluminum oxide domains will decrease, leading to a decrease in the fraction of O-rich AlO_x and producing a stoichiometric shift from high oxygen content for early cycle numbers to lower oxygen content for increased cycle numbers. This behavior is consistent with the trend in O/Al *vs* the number of growth cycles we observe in Table 1, where the value of the O/Al ratio decreases with an increasing number of ALD cycles.

The trends in CN values reported in Table 1 further support our proposed model of an oxygen-rich boundary layer on the ALD aluminum oxide. We observe that the Al−O CN increases from a value of 4.58 at 75cTMA/H_2O up to a value of 4.67 at 150cTMA/H_2O. All of the Al−O values for ALD grown AlO_x in Table 1 are lower than the theoretical values for θ-Al_2O_3 and α-$Al(OH)_3$. The θ-Al_2O_3 structure has a 1:1 blend of Al−O tetrahedra (CN of 4) and Al−O octahedra (CN of 6) to yield an average Al−O CN of 5, while α-$Al(OH)_3$ contains only Al−O octahedra and has a theoretical CN of 6. Based on the O-rich surface model depicted in Figure 3a, we expect surface Al to have a CN as low as 3. For fewer ALD cycles, a larger fraction of the material will be in the surface boundary layer, driving smaller Al−O CNs for fewer ALD cycles, as we observe here. Likewise, in the O-rich surface layer, we expected an O−Al CN of 1−2, *versus* a value of 3.5 for bulk θ-Al_2O_3, such that fewer ALD cycles will yield smaller O−Al CNs. Indeed, we observe that the O−Al CN also increases from a value of 2.76 for 75cTMA/H_2O up to a value of 2.88 for 150cTMA/H_2O, in line with expectations for the model in Figure 3.

To evaluate how well the simple model depicted in Figure 3b captures the experimental data in Table 1, we calculate predicted values of the metrics in Table 1 based on this core−shell model with some simple assumptions. For this analysis, we assume spherical nanoparticle domains of aluminum oxide, where the particle diameter increases with increasing film thickness, and the O-rich region is a spherical shell of constant

https://dx.doi.org/10.1021/acsami.0c01905
ACS Appl. Mater. Interfaces 2020, 12, 22804−22814

thickness, δ. We assume that the O-rich region is limited to one monolayer and we assume a value of δ = 3 Å based on the expected thickness for a monolayer of θ-Al_2O_3. In the O-rich shell region, we assume that the O/Al ratio is 3 and the Al−O CN is 3. For the bulk Al_2O_3 on the interior of the spherical particle, we assume that the O/Al ratio is 1.5, the Al−O CN is 5, and the O−Al CN is 3.5, corresponding to bulk θ-Al_2O_3. For a particle with a radius of 15 nm (consistent with TEM observations for 100cTMA/H_2O in Figure 1a), we calculate average values of O/Al = 1.588, Al−O CN 4.88, and O−Al CN = 3.35 using this model. These values are close (4% lower, 6% higher, and 20% higher, respectively) to the values of O/Al = 1.658, Al−O CN = 4.62, and O−Al CN = 2.79 reported in Table 1 for 100cTMA/H_2O. The modeled values for O/Al and Al−O agree closely with measured values, and as we adjust the particle diameter in the model, the trends we observe are in general agreement with our experimental values, supporting our interpretation of the data in Table 1. By allowing the values for the thickness of the O-rich layer, CNs in bulk Al_2O_3, and particle radii of the AlO_x particles for the 75cTMA/H_2O and 150cTMA/H_2O to vary and performing an optimization to minimize the model error across all three growth samples, we arrive at predicted values of δ = 5.4 Å, Al−O CN = 4.80, and O−Al CN = 3.00 within the bulk aluminum oxide and average particle radii of 14 and 21 nm for the 75cAl_2O_3 and 150cAl_2O_3 coatings, respectively. These values result in <1% error for all of the metrics reported in Table 1 and further support the interpretation that the variation in structural metrics arises from multiphase behavior.

Although the samples described above provide some initial insights into the structure of ALD AlO_x at varying domain sizes, the interpretation cannot provide insights into the structural evolution of the film during growth. Understanding how the structure of the ALD films evolves during deposition, especially at early cycle numbers, is expected to provide insights into the process−structure−property relationships of ALD films which are inaccessible using *ex situ* measurements. To accomplish this, we performed *in operando* HE-XRD coupled to PDF analysis using a modular and mobile ALD reactor reported previously.[52] A new reactor chamber was specially constructed to allow for HE-XRD measurements during ALD growth on a powder sample within a polyimide capillary, as depicted in Figure 4. The reactor body is depicted in Figure 4a. In Figure 4b is a schematic depicting the cross section of a polyimide capillary filled with CNTs and the X-ray path. We note that for these experiments, we employed hydroxyl-terminated CNTs to allow for facile nucleation and uniform layers without the need for a NO_2/TMA nucleation layer used in the samples in Figure 1 mentioned above. The assembled reactor with polyimide windows in place is depicted in Figure 4c. An overall view of the HE-XRD reactor is depicted in Figure 4d with the locations of the entering X-ray beam, gas inlet and outlet, 2D area detector, and capillary indicated. The gas inlet and outlet are connected *via* flexible hoses to the mobile reactor reported previously.[52]

Using this reactor, we performed HE-XRD after each TMA/H_2O ALD cycle up to 50 ALD cycles. Shown in Figure 5 are experimental PDFs derived from HE-XRD patterns acquired *in operando* during ALD growth. In Figure 5a are PDFs for every five ALD cycles up to 50 cycles, and in Figure 5b is a heat map plot showing PDF data for every ALD cycle from 5 up to 50. We note that during the first three ALD cycles, we visually observed that the CNT powder underwent significant bulk

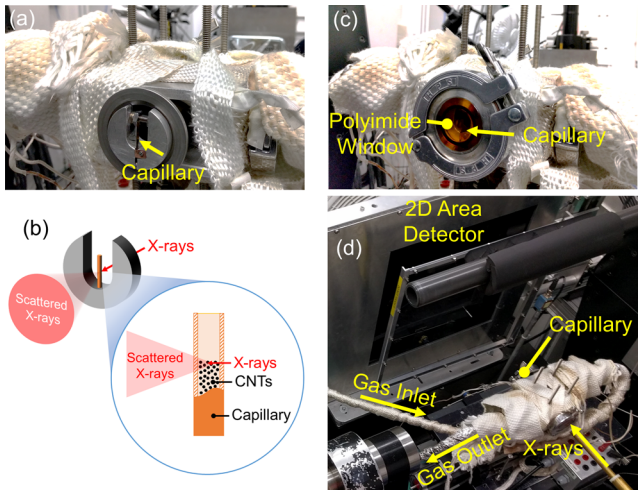

Figure 4. Custom ALD reactor for *in operando* HE-XRD measurement and PDF analysis consisting of (a) a KF-40 cross with a custom insert to hold a polyimide capillary, which was (b) filled with a powder substrate and (c) sealed using polyimide windows that provided >45° diffraction angle for (d) PDF HE-XRD measurement during ALD growth.

motion before settling by the third ALD cycle. We expect that this motion may arise from the increase in temperature and pressure upon reaction of TMA with the CNTs to form methane. As the mass of the CNTs increased with the ALD coating, the motion of the particles during the reaction diminishes. Because of this motion, we used the fourth ALD cycle as the background reference for evaluating the PDFs from the HE-XRD data. Consistent with the data reported above in Figure 1, we observe no long-range order in the ALD AlO_x from *in operando* measurements in Figure 5—for all ALD cycle numbers, we observe no peaks beyond a pair distance of about 5 Å. We also observe that in Figure 5a, the peak heights (and therefore the local atomic structure) change with the number of ALD cycles. For example, we see that after five ALD cycles there is a small peak at 1.8 Å, which increases with the cycle number up to 50 cycles. We note that the features at ∼3 Å in Figure 5a are qualitatively different from the data reported in Figures 1 and 2 mentioned above. This may arise because the substrate surface is different here (hydroxyl-terminated CNTs *vs* bare CNTs in Figure 1), because the number of ALD cycles is different (≥75 ALD cycles in Figures 1 and 2 *vs* ≤ 50 cycles in Figure 5), or because of differences in sample age/storage conditions. The data in Figure 5 are collected *in operando* without breaking vacuum, whereas the data in Figure 1 are collected *ex situ* after the samples had been exposed to long-term atmospheric conditions.

The ability to perform HE-XRD after each precursor exposure allows us to analyze the local atomic structure during nucleation and growth of ALD aluminum oxide. We performed stochastic structure fits for each PDF trace reported in Figure 5a (every five ALD cycles), and in Figure 6, we report experimental values of O/Al, Al−O bond length, Al−O CN, and O−Al CN derived from statistical analysis of these stochastic structural models. We observe that as the number of ALD growth cycles increases from 5 to 50 cycles, we observe a decrease in the O/Al ratio from 1.889 to 1.584, as shown in Figure 6a, and a decrease in the Al−O bond length from 1.844 to 1.808 Å, as shown in Figure 6b. We note that the value of Al−O CN at five ALD cycles was omitted from Figure 6c

https://dx.doi.org/10.1021/acsami.0c01905
ACS Appl. Mater. Interfaces 2020, 12, 22804−22814

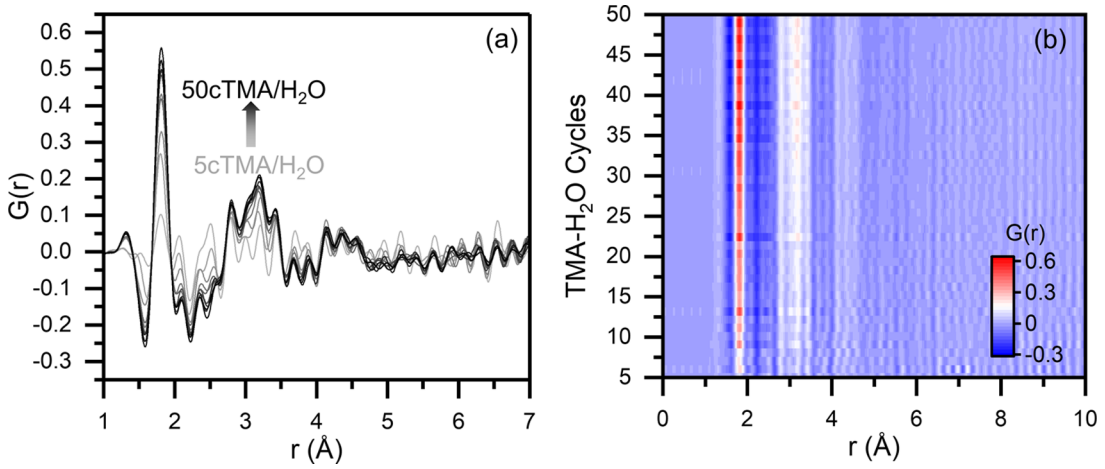

Figure 5. PDFs calculated from *in operando* HE-XRD data during TMA/H_2O ALD growth and plotted (a) for every five ALD cycles, and (b) heat map plot showing the evolution of the PDF for every ALD cycle from 5 to 50 ALD cycles compiled using the scedasticity software package.[53]

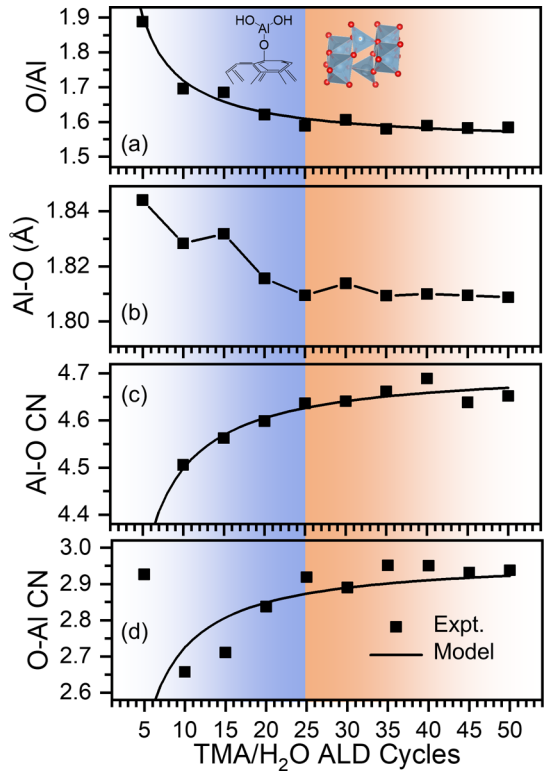

Figure 6. Local structural metrics derived from stochastic modeling of *in operando* PDF measurements during TMA/H_2O ALD growth from 5 to 50 ALD cycles including (a) O/Al stoichiometric ratio, (b) Al−O bond length, (c) Al−O CN, and (d) O−Al CN. The solid lines are model fits using the simple model depicted in Figure 3.

because it was significantly off the scale and obfuscated the trend from 10 to 50 ALD cycles if it was included. For reference, the value of the Al−O CN after five ALD cycles was 4.835. The Al−O and O−Al CNs at five ALD cycles are distinct from the trend for the other ALD cycles. From 10 to 50 ALD cycles, we observe an increase in the Al−O CN from 4.506 to 4.652, as shown in Figure 6c, and an increase in the O−Al CN from 2.658 to 2.937, as shown in Figure 6d. Apart from the CN data at five ALD cycles, the trends observed in the metrics in Figure 6 appear to be consistent with the simple structural model proposed above in Figure 3, where an Al_2O_3 internal volume is surrounded by an O-rich exterior layer. At low ALD cycle numbers, highlighted in blue in Figure 6, the values of these structural metrics are more consistent with the O-rich boundary layer, represented by the inset at the left of Figure 6a, with ideal values of O/Al of 3, Al−O CN of 3, and O−Al CN of 1, as reported in Table 1 mentioned above. At higher cycle numbers, highlighted in orange in Figure 6, the structural metrics approach steady-state values more consistent with bulk θ-Al_2O_3, represented by the inset at the right of Figure 6a, with an O/Al of 1.5, Al−O CN of 5, and O−Al CN of 3.5, as reported in Table 1 mentioned above.

We performed an equivalent analysis to the one outlined above and fit the experimental data in Figure 6a,c,d using the O-rich interface model, in Figure 3, to determine values of δ and the CNs in the bulk ALD AlO_x. In order to perform this model fit, we needed thickness estimates for each number of ALD cycles. We performed TEM on the CNTs following the *in operando* HE-XRD and measured a final aluminum oxide film thickness of 14 nm ± 1 nm (not shown). We assumed a constant growth rate to reach this final thickness (2.8 Å/cycle) and used this growth rate to calculate thicknesses for each number of ALD cycles. We note that the growth rate of 2.8 Å/cycle is higher than values of 1−2 Å/cycle in previous studies[44,54−56] and may indicate a CVD component to the growth with the reactor chamber and dosing conditions employed in this work. Assuming values of Al−O CN = 3, O−Al CN = 1, and O/Al = 3 for the O-rich outer layer, the model fit yielded predicted values of δ = 1.8 Å, O/Al = 1.536, Al−O CN = 4.71, and O−Al CN = 2.97 in the bulk aluminum oxide. The Al−O CN and O−Al CN values are remarkably close to the values determined by fitting the data, as shown above in Table 1, despite differences in nucleation and growth modes with the different CNT substrates. We plot predicted average O/Al, Al−O CN, and O−Al CN *vs* the number of ALD cycles based on this O-rich boundary layer model, as shown in Figure 6a,c,d as solid lines. The O-rich boundary layer model largely captures the trends in structural metrics during ALD growth reported in Figure 6 and further supports this interpretation of the experimental trends.

We note that the fitted value of the thickness of the O-rich surface layer δ = 1.8 Å determined from the *in operando* measurements is significantly lower than the value δ = 5.4 Å determined from the *ex situ* data mentioned above. We expect

https://dx.doi.org/10.1021/acsami.0c01905
ACS Appl. Mater. Interfaces 2020, 12, 22804−22814

that because the *ex situ* samples had been exposed to the atmosphere, water in the atmosphere caused a larger extent of surface hydrolysis giving rise to more surface hydroxyls and driving a larger model value of δ for the *ex situ* samples. We also note that the Al−O and O−Al CNs measured for five ALD cycles of TMA/H_2O diverge from the trends from 10 to 50 ALD cycles and from the O-rich surface model. The values derived from our experimental data are Al−O CN = 4.84 and O−Al CN = 2.93, whereas the O-rich model predicts values of Al−O CN = 4.28 and O−Al CN = 2.48. This deviation likely arises from high-energy dangling bonds driving clustering and leading to higher coordination during sub-monolayer growth. In general, the simple O-rich surface model we propose fits the experimental data reasonably well and helps reconcile the trends we observe in stoichiometry and CNs from 10 to 50 ALD cycles.

Interestingly, we observe smaller-than-expected values of the Al−O bond length for all samples. The Al−O bond length, as shown in Figure 6b, after 10 ALD cycles is found to be 1.832 Å and decreases to a value of 1.809 Å at 50 ALD cycles. An examination of the Al−O two-body pair potential established for amorphous aluminum oxides in prior work[57] suggests that the lowest energy Al−O pair distance occurs at ∼1.9 Å and that a decrease in bond length from 1.9 to 1.8 Å amounts to an increase in energy by 2 kcal/mol per Al−O bond. This would suggest that for these ALD aluminum oxide films grown on hydroxyl-terminated CNTs, the Al−O bond lengths are under compressive strain up to 50 ALD cycles. Indeed, the average bond length values for ideal θ-Al_2O_3 and α-$Al(OH)_3$ are 1.87 and 1.90 Å, respectively—significantly longer than the average Al−O bond lengths measured here for ALD aluminum oxide. However, we note that the shorter Al−O bond lengths we observe in ALD-grown aluminum oxide agree well with the average Al−O bond length for tetrahedral AlO_4 groups, which are 1.70−1.79 Å within the θ-Al_2O_3 structure.[46] This would indicate that Al is largely tetrahedrally coordinated in ALD-grown aluminum oxide. The Al−O CN values in Figure 6c agree with this conclusion and suggest an excess of tetrahedra *versus* octahedra, where all of the average Al−O CN values in Figure 6c are <4.7, corresponding to >65% tetrahedra for up to 50 ALD cycles. We also note that the Al−O bond lengths and coordination environments we observe for ALD AlO_x are in close agreement with results observed in liquid aluminum oxide at high temperatures.[58,59] We expect that the formation of a tetrahedra-rich aluminum oxide phase with short Al−O bonds is somehow driven by as-yet undescribed mechanistic bias of the ALD growth mechanism toward tetrahedral Al centers. The short Al−O bond lengths we observe are in apparent disagreement with previous reports indicating that ALD AlO_x is under intrinsic tensile strain.[60,61] This discrepancy may arise because of the curved nanoscale (∼20 nm diameter) CNT substrate surface employed here *versus* flat substrates in prior work or because the coatings we study here are much thinner than coatings studied in these previous reports.

3. CONCLUSIONS

In this work, we employ HE-XRD and PDF analysis to provide insight into the atomic-scale structural features of amorphous aluminum oxide grown by ALD. By performing stochastic structural modeling to fit experimental PDF data, we quantify structural metrics for the ALD aluminum oxide and we identify significant deviations from ideal aluminum oxide crystal structures. Compared with ideal crystal structures of Al_2O_3, we observe that ALD aluminum oxide is oxygen-rich and exhibits a lower average Al−O CN and a shorter average Al−O bond length. Additionally, these structural features vary dynamically with the number of ALD cycles. We propose a simple two-phase model to explain these variations. This model consists of a bulk ALD aluminum oxide phase that grows with the number of ALD cycles, surrounded by a surface/interface layer of constant thickness. This simple model captures the qualitative trends we observe in the structural metrics for both nanosphere and thin-film ALD aluminum oxide morphologies with increasing ALD cycle numbers.

Broadly, this work also provides a new lens through which we examine previous studies employing ALD AlO_x. Although some reports have achieved outstanding performance using ALD AlO_x coatings, an untold number of attempts to use ALD AlO_x for new applications have not achieved the desired outcome and were never submitted for publication. An explanation for why ALD AlO_x works in some instances and not in others is lacking. Although many factors beyond the ALD AlO_x atomic structure may play a role in any individual application, the impact of the ALD AlO_x atomic structure on material performance is a central and largely unanswered question in this area. The work we report here establishes that we should not assume that all ALD AlO_x is structurally equivalent but rather ALD AlO_x exhibits varying atomic structure depending on the process conditions (*e.g.*, substrates and the number of ALD cycles). Understanding specific differences in the atomic structure of ALD aluminum oxide with the substrate, thickness and other process conditions is expected to help reconcile disparate outcomes that have been observed for the use of ALD aluminum oxide in a range of applications.[1−7] The HE-XRD and PDF analysis we demonstrate—especially the *in operando* HE-XRD during ALD growth—provide a platform to characterize the atomic structure of amorphous ALD layers and open a pathway to establishing process−structure−property relationships for ALD-grown amorphous materials. We note that although the present work demonstrates PDF measurements on powder samples, future work will be able to take advantage of recently developed grazing incident PDF measurement capability[43] to simplify the study of ALD coatings using PDF measurements and analysis on planar samples.

4. MATERIALS AND METHODS

4.1. *Ex Situ* HE-XRD. *Ex situ* HE-XRD was performed at 6-ID-D at the Advanced Photon Source (APS) at Argonne National Laboratory (ANL) using an X-ray wavelength of 0.1236 Å. For initial demonstration of HE-XRD on ALD samples, we employed multi-walled CNT (Nanocyl 7000 series) samples coated with aluminum oxide ALD as reported in prior work.[44] CNTs were coated with ALD Al_2O_3 using TMA and water (H_2O). We studied CNTs with no pretreatment and CNTs coated with 50 cycles of NO_2/TMA as the nucleation layer prior to the ALD coating. Both samples were coated in a static dose configuration at 180 °C. The ALD-coated CNTs were loaded into 1 mm diameter polyimide capillaries and evaluated using HE-XRD.

4.2. *In Operando* HE-XRD during ALD. *In operando* HE-XRD during ALD growth was performed at 11-ID-C at APS using an X-ray wavelength of 0.1173 Å. *In operando* measurements were performed using a custom modular ALD reactor described previously[52] with a sample stage specifically designed for *in operando* HE-XRD on powders, as discussed below and depicted in Figure 4. This stage employed a KF40 cross with precursor flow across one straight path in

https://dx.doi.org/10.1021/acsami.0c01905
ACS Appl. Mater. Interfaces 2020, 12, 22804−22814

the cross and X-ray beam transmission through polyimide windows in the other straight path of the cross. A custom insert was constructed to nest within the KF40 tube and hold a polyimide capillary filled with powder under vacuum and fixed within the X-ray beam during precursor exposures. We employed polyimide capillaries to minimize background scattering and allow for experiments at elevated temperatures (>150 °C). We sealed the base of the capillary with high-temperature epoxy and left the top of the capillary unsealed to allow the precursors to transport into the capillary and react at the CNTs. The polyimide capillary was located immediately adjacent to the polyimide window on the X-ray beam exit to allow X-rays which diffracted off the powder sample to pass through the polyimide window at diffraction angles of up to ∼45°. Here, the hydroxyl-functionalized multiwalled CNT (CNT-OH, nano-amorphous materials, 10−20 nm diameter, 10−30 μm length, 95%) were employed to facilitate ALD nucleation without requiring NO_2/TMA pretreatment.

Prior to diffraction measurements, the sample stage was scanned in the directions orthogonal to the X-ray beam to locate the CNT−OH-filled capillary. The sample stage was positioned such that the X-ray beam impinged on the top portion of the CNT-OHs within the polyimide capillary to ensure that the X-ray beam was probing saturated ALD chemistry. We note that the potential for accumulation and release of precursors and byproducts within the bulk CNT-OH powder is one shortcoming of the approach employed here. This could be remedied in future work by employing grazing incidence PDF measurements on planar substrates which have recently been demonstrated.[43] Long purge times were employed following each precursor exposure and between deposition cycles to allow for excess precursors and reaction byproducts to transport out through the CNT-OHs along the length of the polyimide capillary and mitigate any precursor or byproduct accumulation in the CNT-OHs. The vacuum chamber was maintained at 150 °C using PID temperature controllers and operated at ∼1 Torr of nitrogen carrier gas flow. Precursors were dosed in TMA-purge−water-purge cycles where one cycle consisted of a 10 s TMA exposure, a 120 s nitrogen purge, a 10 s water exposure, and a 120 s nitrogen purge. HE-XRD measurements were collected between ALD cycles. Following each ALD cycle, deposition was halted until the HE-XRD measurement was complete, and then another deposition cycle was performed. Each HE-XRD measurement consisted of 25 sequential 12 s X-ray exposures (5 min data collection time), which were averaged to produce one HE-XRD pattern for analysis.

4.3. PDF Analysis and Stochastic Modeling. 2D HE-XRD patterns were aligned, integrated over 360° of diffraction angles, and processed into 1D scans of diffraction intensity *vs* momentum transfer (Q) using the GSAS-II software package.[62] PDF analysis of 1D diffraction data was performed using PDFgetX3.[63] Stochastic modeling of PDF data was performed using fullrmc.[64] A simulation box consisting of a supercell of θ-Al_2O_3 with 4 nm along each edge was employed as a starting point for stochastic fitting. fullrmc employs a stochastic modeling technique in which automated and guided structural and geometrical changes are made to an atomic/molecular structure model until it has the greatest consistency with a set of experimental (PDF) data.[64,65] Each fullrmc fitting run consisted of >6 × 10^6 structural perturbations composed of both translation and atom removal steps. We note that the "AtomsRemoveGenerator" which enables atom removal within fullrmc software was specifically developed for this work and was employed to predict the Al/O stoichiometry. Statistical analysis of the resulting atomistic model provides a range of structural information including material composition, bonding, and atomic coordination.[66]

AUTHOR INFORMATION

Corresponding Authors

Matthias J. Young − *Department of Biomedical, Biological, and Chemical Engineering and Department of Chemistry, University of Missouri, Columbia 65211, Missouri, United States; Applied Materials Division, Argonne National Laboratory, Lemont 60439, Illinois, United States;* orcid.org/0000-0001-7384-4333; Email: matthias.young@missouri.edu

Jeffrey W. Elam − *Applied Materials Division, Argonne National Laboratory, Lemont 60439, Illinois, United States;* orcid.org/0000-0002-5861-2996; Email: jelam@anl.gov

Authors

Nicholas M. Bedford − *School of Chemical Engineering, University of New South Wales, Sydney 2052, New South Wales, Australia;* orcid.org/0000-0002-4424-7094

Angel Yanguas-Gil − *Applied Materials Division, Argonne National Laboratory, Lemont 60439, Illinois, United States*

Steven Letourneau − *Applied Materials Division, Argonne National Laboratory, Lemont 60439, Illinois, United States;* orcid.org/0000-0002-0007-6940

Matthew Coile − *Applied Materials Division, Argonne National Laboratory, Lemont 60439, Illinois, United States*

David J. Mandia − *Applied Materials Division, Argonne National Laboratory, Lemont 60439, Illinois, United States;* orcid.org/0000-0003-0325-3612

Bachir Aoun − *X-ray Sciences Division, Argonne National Laboratory, Lemont 60439, Illinois, United States*

Andrew S. Cavanagh − *Department of Chemistry, University of Colorado Boulder, Boulder 80309, Colorado, United States;* orcid.org/0000-0002-6201-530X

Steven M. George − *Department of Chemistry, University of Colorado Boulder, Boulder 80309, Colorado, United States;* orcid.org/0000-0003-0253-9184

Complete contact information is available at: https://pubs.acs.org/10.1021/acsami.0c01905

Notes

The authors declare no competing financial interest.

ACKNOWLEDGMENTS

This research was supported as part of the Center for Electrochemical Energy Science, an Energy Frontier Research Center funded by the U.S. Department of Energy, Office of Science, Office of Basic Energy Sciences. The use of the 6-ID-D and 11-ID-C beamlines of the Advanced Photon Source is also supported under Contract DE-AC02-06CH11357. We would like to thank Chris Benmore and Doug Robinson for assistance with HE-XRD experiments at 6-ID-D and Uta Ruett, Olaf Borkiewicz, Yang Ren, Richard Spence, Kevin Beyer, Guy Jennings, Andrey Yakovenko, and Charles Kurtz for assistance with *in operando* measurements at 11-ID-C. We also thank Prof. C. Michael Greenlief at the University of Missouri for insightful discussion regarding the use of NMR to characterize ALD films.

REFERENCES

(1) O'Neill, B. J.; Jackson, D. H. K.; Lee, J.; Canlas, C.; Stair, P. C.; Marshall, C. L.; Elam, J. W.; Kuech, T. F.; Dumesic, J. A.; Huber, G. W. Catalyst Design with Atomic Layer Deposition. *ACS Catal.* **2015**, *5*, 1804−1825.

(2) Xu, S.; Kim, Y.; Park, J.; Higgins, D.; Shen, S.-J.; Schindler, P.; Thian, D.; Provine, J.; Torgersen, J.; Graf, T.; Schladt, T. D.; Orazov, M.; Liu, B. H.; Jaramillo, T. F.; Prinz, F. B. Extending the Limits of Pt/C Catalysts with Passivation-Gas-Incorporated Atomic Layer Deposition. *Nat. Catal.* **2018**, *1*, 624−630.

(3) Jung, Y. S.; Cavanagh, A. S.; Riley, L. a.; Kang, S.-H.; Dillon, A. C.; Groner, M. D.; George, S. M.; Lee, S.-H. Ultrathin Direct Atomic Layer Deposition on Composite Electrodes for Highly Durable and Safe Li-Ion Batteries. *Adv. Mater.* **2010**, *22*, 2172−2176.

(4) Meng, X.; Yang, X.-Q.; Sun, X. Emerging Applications of Atomic Layer Deposition for Lithium-Ion Battery Studies. *Adv. Mater.* **2012**, *24*, 3589−3615.
(5) Gu, J.; Yan, Y.; Young, J. L.; Steirer, K. X.; Neale, N. R.; Turner, J. A. Water Reduction by a p-$GaInP_2$ Photoelectrode Stabilized by an Amorphous TiO_2 Coating and a Molecular Cobalt Catalyst. *Nat. Mater.* **2015**, *15*, 456−460.
(6) Su, J.; Li, Z.; Yu, Y.; Wang, X. Atomic Layer Deposition for Advanced Electrode Design in Photoelectrochemical and Triboelectric Systems. *Adv. Mater. Interfaces* **2017**, *4*, 1600835.
(7) Shearrow, A.; Koolstra, G.; Whiteley, S. J.; Earnest, N.; Barry, P. S.; Heremans, F. J.; Awschalom, D. D.; Shirokoff, E.; Schuster, D. I. Atomic Layer Deposition of Titanium Nitride for Quantum Circuits. *Appl. Phys. Lett.* **2018**, *113*, 212601.
(8) *ALD Nano Now Coats Tons of Particles Per Day*; ALD Nanosolutions ENEWS, 2017; Vol. 2 (3).
(9) Miikkulainen, V.; Leskelä, M.; Ritala, M.; Puurunen, R. L. Crystallinity of Inorganic Films Grown by Atomic Layer Deposition: Overview and General Trends. *J. Appl. Phys.* **2013**, *113*, 021301.
(10) Groner, M. D.; Fabreguette, F. H.; Elam, J. W.; George, S. M. Low-Temperature Al_2O_3 Atomic Layer Deposition. *Chem. Mater.* **2004**, *16*, 639−645.
(11) Jakschik, S.; Schroeder, U.; Hecht, T.; Krueger, D.; Dollinger, G.; Bergmaier, A.; Luhmann, C.; Bartha, J. W. Physical Characterization of Thin ALD-Al_2O_3 Films. *Appl. Surf. Sci.* **2003**, *211*, 352−359.
(12) Wind, R. A.; George, S. M. Quartz Crystal Microbalance Studies of Al_2O_3 Atomic Layer Deposition Using Trimethylaluminum and Water at 125 °C. *J. Phys. Chem. A* **2010**, *114*, 1281−1289.
(13) Puurunen, R. L. Surface Chemistry of Atomic Layer Deposition: A Case Study for the Trimethylaluminum/Water Process. *J. Appl. Phys.* **2005**, *97*, 121301.
(14) Guerra-Nuñez, C.; Döbeli, M.; Michler, J.; Utke, I. Reaction and Growth Mechanisms in Al_2O_3 Deposited via Atomic Layer Deposition: Elucidating the Hydrogen Source. *Chem. Mater.* **2017**, *29*, 8690−8703.
(15) Matero, R.; Rahtu, A.; Ritala, M.; Leskelä, M.; Sajavaara, T. Effect of Water Dose on the Atomic Layer Deposition Rate of Oxide Thin Films. *Thin Solid Films* **2000**, *368*, 1−7.
(16) Nilsen, O.; Fjellvåg, H.; Kjekshus, A. Growth of Manganese Oxide Thin Films by Atomic Layer Deposition. *Thin Solid Films* **2003**, *444*, 44−51.
(17) Tallarida, M.; Kukli, K.; Michling, M.; Ritala, M.; Leskelä, M.; Schmeisser, D. Substrate Reactivity Effects in the Atomic Layer Deposition of Aluminum Oxide from Trimethylaluminum on Ruthenium. *Chem. Mater.* **2011**, *23*, 3159−3168.
(18) Yao, Y.; Coyle, J. P.; Barry, S. T.; Zaera, F. Effect of the Nature of the Substrate on the Surface Chemistry of Atomic Layer Deposition Precursors. *J. Chem. Phys.* **2017**, *146*, 052806.
(19) Naumann, V.; Otto, M.; Wehrspohn, R. B.; Hagendorf, C. Chemical and Structural Study of Electrically Passivating Al_2O_3/Si Interfaces Prepared by Atomic Layer Deposition. *J. Vac. Sci. Technol., A* **2012**, *30*, 04D106−6.
(20) Ritala, M.; Leskelä, M.; Dekker, J.-P.; Mutsaers, C.; Soininen, P. J.; Skarp, J. Perfectly Conformal TiN and Al_2O_3 Films Deposited by Atomic Layer Deposition. *Chem. Vap. Deposition* **1999**, *5*, 7−9.
(21) Sneh, O.; Clark-Phelps, R. B.; Londergan, A. R.; Winkler, J.; Seidel, T. E. Thin Film Atomic Layer Deposition Equipment for Semiconductor Processing. *Thin Solid Films* **2002**, *402*, 248−261.
(22) Ott, A. W.; Klaus, J. W.; Johnson, J. M.; George, S. M. Al_2O_3 Thin Film Growth on Si(100) Using Binary Reaction Sequence Chemistry. *Thin Solid Films* **1997**, *292*, 135−144.
(23) Groner, M. D.; Elam, J. W.; Fabreguette, F. H.; George, S. M. Electrical Characterization of Thin Al_2O_3 Films Grown by Atomic Layer Deposition on Silicon and Various Metal Substrates. *Thin Solid Films* **2002**, *413*, 186−197.
(24) Jensen, J. M.; Oelkers, A. B.; Toivola, R.; Johnson, D. C.; Elam, J. W.; George, S. M. X-Ray Reflectivity Characterization of ZnO/Al_2O_3 Multilayers Prepared by Atomic Layer Deposition. *Chem. Mater.* **2002**, *14*, 2276−2282.
(25) Rayner, B.; Niimi, H.; Johnson, R.; Therrien, B.; Lucovsky, G.; Galeener, F. L. Spectroscopic Evidence for a Network Structure in Plasma-Deposited Ta_2O_5 Films for Microelectronic Applications. *AIP Conference Proceedings; AIP*, 2001; Vol. *550*, pp 149−153.
(26) Lucovsky, G.; Rozaj-Brvar, A.; Davis, R. F. An XPS Study of Oxide Glasses Containing Al. *The Structure of Non-Crystalline Materials*; 1982; pp 193−205.
(27) Lee, S. K.; Lee, S. B.; Park, S. Y.; Yi, Y. S.; Ahn, C. W. Structure of Amorphous Aluminum Oxide. *Phys. Rev. Lett.* **2009**, *103*, 095501.
(28) Young, M. J.; Hare, C. D.; Cavanagh, A. S.; Musgrave, C. B.; George, S. M. Rapid Growth of Crystalline Mn_5O_8 by Self-Limited Multilayer Deposition Using $Mn(EtCp)_2$ and O_3. *ACS Appl. Mater. Interfaces* **2016**, *8*, 18560−18569.
(29) Pallister, P. J.; Barry, S. T. Surface Chemistry of Group 11 Atomic Layer Deposition Precursors on Silica Using Solid-State Nuclear Magnetic Resonance Spectroscopy. *J. Chem. Phys.* **2017**, *146*, 052812.
(30) Han, B.; Key, B.; Lipton, A. S.; Vaughey, J. T.; Hughes, B.; Trevey, J.; Dogan, F. Influence of Coating Protocols on Alumina-Coated Cathode Material: Atomic Layer Deposition versus Wet-Chemical Coating. *J. Electrochem. Soc.* **2019**, *166*, A3679−A3684.
(31) Lakomaa, E.-L.; Root, A.; Suntola, T. Surface Reactions in Al_2O_3 Growth from Trimethylaluminium and Water by Atomic Layer Epitaxy. *Appl. Surf. Sci.* **1996**, *107*, 107−115.
(32) Kimoto, K.; Matsui, Y.; Nabatame, T.; Yasuda, T.; Mizoguchi, T.; Tanaka, I.; Toriumi, A. Coordination and Interface Analysis of Atomic-Layer-Deposition Al_2O_3 on Si(001) Using Energy-Loss near-Edge Structures. *Appl. Phys. Lett.* **2003**, *83*, 4306−4308.
(33) Nakamura, R.; Ishimaru, M.; Yasuda, H.; Nakajima, H. Atomic Rearrangements in Amorphous Al_2O_3 under Electron-Beam Irradiation. *J. Appl. Phys.* **2013**, *113*, 064312.
(34) Proffen, T.; Billinge, S. J. L.; Egami, T.; Louca, D. Structural Analysis of Complex Materials Using the Atomic Pair Distribution Function — a Practical Guide. *Z. Kristallogr.—Cryst. Mater.* **2003**, *218*, 132−143.
(35) Petkov, V. Nanostructure by High-Energy X-Ray Diffraction. *Mater. Today* **2008**, *11*, 28−38.
(36) Tulk, C. A.; Benmore, C. J.; Urquidi, J.; Klug, D. D.; Neuefeind, J.; Tomberli, B.; Egelstaff, P. A. Structural Studies of Several Distinct Metastable Forms of Amorphous Ice. *Science* **2002**, *297*, 1320−1324.
(37) Billinge, S. J. L.; Kanatzidis, M. G. Beyond Crystallography: The Study of Disorder, Nanocrystallinity and Crystallographically Challenged Materials with Pair Distribution Functions. *Chem. Commun.* **2004**, *7*, 749−760.
(38) Kwei, G. H.; Louca, D.; Billinge, S. J. L.; Rosenfeld, H. D. Recent "Local" Structural Studies: Metallic Alloys, Superconductors and Proteins. *Local Structure from Diffraction*; Springer, 1998; pp 323−336.
(39) Bedford, N. M.; Ramezani-Dakhel, H.; Slocik, J. M.; Briggs, B. D.; Ren, Y.; Frenkel, A. I.; Petkov, V.; Heinz, H.; Naik, R. R.; Knecht, M. R. Elucidation of Peptide-Directed Palladium Surface Structure for Biologically Tunable Nanocatalysts. *ACS Nano* **2015**, *9*, 5082−5092.
(40) Letourneau, S.; Young, M. J.; Bedford, N. M.; Ren, Y.; Yanguas-Gil, A.; Mane, A. U.; Elam, J. W.; Graugnard, E. Structural Evolution of Molybdenum Disulfide Prepared by Atomic Layer Deposition for Realization of Large Scale Films in Microelectronic Applications. *ACS Appl. Nano Mater.* **2018**, *1*, 4028−4037.
(41) Jensen, K. M. Ø.; Blichfeld, A. B.; Bauers, S. R.; Wood, S. R.; Dooryhée, E.; Johnson, D. C.; Iversen, B. B.; Billinge, S. J. L. Demonstration of Thin Film Pair Distribution Function Analysis (TfPDF) for the Study of Local Structure in Amorphous and Crystalline Thin Films. *IUCrJ* **2015**, *2*, 481−489.
(42) Shyam, B.; Stone, K. H.; Bassiri, R.; Fejer, M. M.; Toney, M. F.; Mehta, A. Measurement and Modeling of Short and Medium Range Order in Amorphous Ta_2O_5 Thin Films. *Sci. Rep.* **2016**, *6*, 1−7.
(43) Dippel, A.-C.; Roelsgaard, M.; Boettger, U.; Schneller, T.; Gutowski, O.; Ruett, U. Local Atomic Structure of Thin and Ultrathin Films via Rapid High-Energy X-Ray Total Scattering at Grazing Incidence. *IUCrJ* **2019**, *6*, 290−298.

https://dx.doi.org/10.1021/acsami.0c01905
ACS Appl. Mater. Interfaces 2020, 12, 22804−22814

(44) Cavanagh, A. S.; Wilson, C. A.; Weimer, A. W.; George, S. M. Atomic Layer Deposition on Gram Quantities of Multi-Walled Carbon Nanotubes. *Nanotechnology* **2009**, *20*, 255602.
(45) Young, M. J.; Musgrave, C. B.; George, S. M. Growth and Characterization of Al_2O_3 Atomic Layer Deposition Films on sp^2-Graphitic Carbon Substrates Using NO_2/Trimethylaluminum Pretreatment. *ACS Appl. Mater. Interfaces* **2015**, *7*, 12030−12037.
(46) Yamaguchi, G.; Yasui, I.; Chiu, W.-C. A New Method of Preparing θ-Alumina and the Interpretation of Its X-Ray-Powder Diffraction Pattern and Electron Diffraction Pattern. *Bull. Chem. Soc. Jpn.* **1970**, *43*, 2487−2491.
(47) Zigan, F.; Joswig, W.; Burger, N. Die Wasserstoffpositionen Im Bayerit, $Al(OH)_3$. *Z. Kristallogr.—Cryst. Mater.* **1978**, *148*, 10−12.
(48) Levin, I.; Brandon, D. Metastable Alumina Polymorphs: Crystal Structures and Transition Sequences. *J. Am. Ceram. Soc.* **2005**, *81*, 1995−2012.
(49) Zhou, R.-S.; Snyder, R. L. Structures and Transformation Mechanisms of the η, γ and θ Transition Aluminas. *Acta Crystallogr., Sect. B: Struct. Sci.* **1991**, *47*, 617−630.
(50) Kronberg, M. L. Plastic Deformation of Single Crystals of Sapphire: Basal Slip and Twinning. *Acta Metall.* **1957**, *5*, 507−524.
(51) Hoex, B.; Gielis, J. J. H.; Van De Sanden, M. C. M.; Kessels, W. M. M. On the c-Si Surface Passivation Mechanism by the Negative-Charge-Dielectric Al_2O_3. *J. Appl. Phys.* **2008**, *104*, 113703−7.
(52) Klug, J. A.; Weimer, M. S.; Emery, J. D.; Yanguas-Gil, A.; Seifert, S.; Schlepütz, C. M.; Martinson, A. B. F.; Elam, J. W.; Hock, A. S.; Proslier, T. A Modular Reactor Design for in Situ Synchrotron X-Ray Investigation of Atomic Layer Deposition Processes. *Rev. Sci. Instrum.* **2015**, *86*, 113901−11.
(53) Aoun, B.; Yu, C.; Fan, L.; Chen, Z.; Amine, K.; Ren, Y. A Generalized Method for High Throughput In-Situ Experiment Data Analysis: An Example of Battery Materials Exploration. *J. Power Sources* **2015**, *279*, 246−251.
(54) Elam, J. W.; Groner, M. D.; George, S. M. Viscous Flow Reactor with Quartz Crystal Microbalance for Thin Film Growth by Atomic Layer Deposition. *Rev. Sci. Instrum.* **2002**, *73*, 2981−2987.
(55) Ferguson, J. D.; Weimer, A. W.; George, S. M. Atomic Layer Deposition of Ultrathin and Conformal Al_2O_3 Films on BN Particles. *Thin Solid Films* **2000**, *371*, 95−104.
(56) Farmer, D. B.; Gordon, R. G. Atomic Layer Deposition on Suspended Single-Walled Carbon Nanotubes via Gas-Phase Noncovalent Functionalization. *Nano Lett.* **2006**, *6*, 699−703.
(57) Vashishta, P.; Kalia, R. K.; Nakano, A.; Rino, J. P. Interaction Potentials for Alumina and Molecular Dynamics Simulations of Amorphous and Liquid Alumina. *J. Appl. Phys.* **2008**, *103*, 083504.
(58) Shi, C.; Alderman, O. L. G.; Berman, D.; Du, J.; Neuefeind, J.; Tamalonis, A.; Weber, J. K. R.; You, J.; Benmore, C. J. The Structure of Amorphous and Deeply Supercooled Liquid Alumina. *Front. Mater.* **2019**, *6*, 1−15.
(59) Skinner, L. B.; Barnes, A. C.; Salmon, P. S.; Hennet, L.; Fischer, H. E.; Benmore, C. J.; Kohara, S.; Weber, J. K. R.; Bytchkov, A.; Wilding, M. C.; Parise, J. B.; Farmer, T. O.; Pozdnyakova, I.; Tumber, S. K.; Ohara, K. Joint diffraction and modeling approach to the structure of liquid alumina. *Phys. Rev. B: Condens. Matter Mater. Phys.* **2013**, *87*, 024201.
(60) Tripp, M. K.; Stampfer, C.; Miller, D. C.; Helbling, T.; Herrmann, C. F.; Hierold, C.; Gall, K.; George, S. M.; Bright, V. M. The Mechanical Properties of Atomic Layer Deposited Alumina for Use in Micro- and Nano-Electromechanical Systems. *Sens. Actuators, A* **2006**, *130−131*, 419−429.
(61) Ylivaara, O. M. E.; Liu, X.; Kilpi, L.; Lyytinen, J.; Schneider, D.; Laitinen, M.; Julin, J.; Ali, S.; Sintonen, S.; Berdova, M.; Haimi, E.; Sajavaara, T.; Ronkainen, H.; Lipsanen, H.; Koskinen, J.; Hannula, S.-P.; Puurunen, R. L. Aluminum Oxide from Trimethylaluminum and Water by Atomic Layer Deposition: The Temperature Dependence of Residual Stress, Elastic Modulus, Hardness and Adhesion. *Thin Solid Films* **2014**, *552*, 124−135.
(62) Toby, B. H.; Von Dreele, R. B. GSAS-II: The Genesis of a Modern Open-Source All Purpose Crystallography Software Package. *J. Appl. Crystallogr.* **2013**, *46*, 544−549.
(63) Juhás, P.; Davis, T.; Farrow, C. L.; Billinge, S. J. L. PDFgetX3: A Rapid and Highly Automatable Program for Processing Powder Diffraction Data into Total Scattering Pair Distribution Functions. *J. Appl. Crystallogr.* **2013**, *46*, 560−566.
(64) Aoun, B. Fullrmc, a Rigid Body Reverse Monte Carlo Modeling Package Enabled with Machine Learning and Artificial Intelligence. *J. Comput. Chem.* **2016**, *37*, 1102−1111.
(65) Dove, M.; Tucker, M.; Wells, S.; Keen, D. Reverse Monte Carlo Methods. *EMU Notes in Mineralogy*; European Mineralogical Union, 2002; Vol. *4*, pp 59−82.
(66) Le Roux, S.; Petkov, V. ISAACS-Interactive Structure Analysis of Amorphous and Crystalline Systems. *J. Appl. Crystallogr.* **2010**, *43*, 181−185.

https://dx.doi.org/10.1021/acsami.0c01905
ACS Appl. Mater. Interfaces 2020, 12, 22804−22814